Contents lists available at ScienceDirect

Case Studies in Chemical and Environmental Engineering

journal homepage:
www.sciencedirect.com/journal/case-studies-in-chemical-and-environmental-engineering

Interfacial engineering approach for enhanced degradation of methylene blue using platinum-coated polystyrene rough particles: Flow-regulated catalytic activity and kinetic modeling☆

Faizan Khan [a], Vishal Singh Pawak [a], Chandra Shekhar [d], Venkateshwar Rao Dugyala [b], Tarak Mondal [a], Manigandan Sabapathy [a,c] ,*

[a] Department of Chemical Engineering, Indian Institute of Technology Ropar, Rupnagar, 140001, Punjab, India
[b] Department of Chemical Engineering, Indian Institute of Science Education and Research, Bhopal, Bhopal, 462066, Madhya Pradesh, India
[c] Centre of Research for Energy Efficiency and Decarbonization (CREED), Indian Institute of Technology Ropar, Rupnagar, 140001, Punjab, India
[d] Department of Biosystems and Soft Matter, Institute of Fundamental Technological Research Polish Academy of Sciences, Poland

ARTICLE INFO

ABSTRACT

This study explores an efficient decontamination strategy using platinum-coated polystyrene rough-particles as a micron-sized catalyst system for decomposing methylene blue (MB), a common organic pollutant. The synthesized nanomaterials were comprehensively characterized using Nanoparticle Tracking Analysis (NTA), Dynamic Light Scattering (DLS), Atomic Force Microscopy (AFM), Scanning Electron Microscopy (SEM), and Transmission Electron Microscopy (TEM), confirming their morphology, size distribution, and surface properties. The decontamination was performed at the air-water interface through an interface trapping method, with enhanced mixing achieved under a controlled flow environment. The experiments were conducted with a circulation speed of 50 RPM, corresponding to a Reynolds number (NR_e) of 1686 and a high particle packing fraction of 0.8. Under these operating conditions, complete degradation of MB was achieved within 30 min, significantly faster than the 75 min required for degradation in the bulk phase. The reaction kinetics were analyzed and found to follow the Langmuir–Hinshelwood model, with an estimated rate constant of 0.018 min^{-1}, indicating efficient surface-mediated catalytic activity. Furthermore, an Artificial Neural Network (ANN) model was developed to validate and predict the degradation kinetics, showing a Root Mean Square Error (RMSE) of 5.5 and a high correlation coefficient (R^2) of 0.9656, confirming the reliability of the predictive model. This interface-assisted, catalyst-based degradation approach demonstrates a promising, reusable, cost-effective, and environmentally friendly solution for advanced wastewater treatment applications.

1. Introduction

The escalating demand for textiles, pharmaceuticals, and other industrial products has led to a substantial increase in the production and usage of synthetic dyes. While these vibrant colorants enhance the aesthetic appeal of various materials, their indiscriminate discharge into natural ecosystems poses significant environmental and health concerns. Methylene blue (MB), a common azo-based dye pollutant, is soluble in water and is often used in the textile industry for dyeing garments, resulting in the generation of polluted effluents containing both organic and inorganic dyes. Despite its advantages, MB's water solubility has adverse effects on both humans and the environment [1–3]. Addressing this formidable challenge requires innovative and sustainable approaches to efficiently remove dye contaminants from aqueous

environments. Nanotechnology has recently experienced substantial growth due to advancements in various fields such as medicine [4], catalysis [5,6], sensing [7,8], photonics [9–11], and wastewater treatment [12–15]. In this context, wet-chemical methods garnered high interest due to their bulk production capacity and tunability in altering nanostructures.

Thus far, several advanced oxidation processes (AOPs) such as photolysis [16,17], ozonation [18], sonochemical [19,20], and heterogeneous Fenton-like catalyst-assisted [13,21] have been effectively used to eliminate the traces of various chemical residues or dye molecules over traditional methods. Despite the advancements in the field of water treatment, the AOPs possess shortcomings such as high energy demand (sono), strict pH range (Fenton), high H_2O_2 consumption

(Fenton/photo-Fenton), and cost of implementation. In the early 20th century, scientists began exploring platinum's potential as a catalyst for various chemical reactions. This led to its incorporation into catalytic converters for platinum ability to catalyze oxidation reactions, a crucial process in water treatment. Platinum nanoparticles, in particular, exhibit exceptional catalytic activity, enabling them to efficiently oxidize organic pollutants and break down complex molecules into harmless substances [22–27].

Recently, our group reported a simple and straightforward method to remove MB and tetracycline using platinum-decorated rough particles in the bulk [13]. The method employed a wet-chemical approach and offers a single-step route to synthesize various sizes of rough particles of polystyrene (PS) surface engineered with platinum nanoparticles. When exposed, these catalytic rough particles exhibit exemplary decomposing characteristics against hydrogen peroxide, which eventually helps generate radicals to remove desired target pollutants from the wastewater stream. This approach is widely employed in various fields, including environmental remediation [28–30], industrial processes [31], and pharmaceutical synthesis [32], to mitigate the adverse effects of pollutants or to enhance the efficiency of chemical reactions.

In the present study, we confined the application of the rough particles to the air–water interface by carefully controlling the precursor concentration to create a dense platinum shell over polystyrene particles. The as-synthesized nanoparticles and rough particles were analyzed using various techniques, including NTA, DLS, AFM, FESEM, and TEM. Controlled circulation at a programmed speed is introduced under a batch condition to improve the mass transfer characteristics. The combined application of rough particles at the air–water interface, aided by controlled circulation, enhances the physicochemical kinetics multi-fold. For instance, at the same concentration of catalyst particles and hydrogen peroxide, the decomposition time achieved by the rough particles at the interface and in the bulk are approximately 30 and 75 min, respectively.

The enhanced physicochemical kinetics achieved by the synergistic action of rough particles at the air–water interface and controlled circulation highlight the need for advanced predictive modeling techniques to enhance such processes. Because of the complex interaction among several variables in catalytic reactions and mass transfer, traditional modeling techniques may not be sufficient in the representation of the dynamics of the system. In this context, a variety of soft computing techniques, including artificial neural networks (ANNs), fuzzy and neuro-fuzzy intelligent systems, and support vector machines, have been widely utilized to model experimental datasets [33–35]. Among these, ANNs have emerged as the most widely utilized computational framework due to their ability to emulate the structure and function of the biological nervous system through numerous interconnected processing units. ANNs are renowned for their capability to perform high-speed parallel information processing, exhibit fault tolerance, and conduct global mapping [36]. In the context of performance prediction and process optimization, predictive modeling using artificial intelligence has become a pivotal area of research, especially for case-specific experimental investigations. However, despite the extensive application of AI tools in various domains, to the best of our knowledge, the use of AI techniques for predictive modeling of MB removal in water treatment processes has yet to be thoroughly explored.

The proposed strategy creates high-surface-area platforms conducive to catalytic reactions by employing rough particles at the air–water interface. This strategic positioning facilitates efficient mass transfer and maximizes the interaction between catalyst and target molecules, thereby accelerating the degradation of MB contaminants. The catalytic degradation of MB at the air–water interface represents a paradigm shift in environmental remediation. There are various advanced oxidation processes that show very good performance in wastewater treatment. However, these AOPs possess shortcomings such as high energy demand, strict pH range, high H_2O_2 consumption, and cost of implementation [13]. The proposed process, platinum-decorated

PS rough colloids at the air–water interface method provides significant advantages through integration of air–water interface such as enhanced surface catalysis, sustainability, and operational feasibility. It presents a novel and scalable approach that addresses some of the key limitations of existing MB removal techniques, making it a valuable advancement in the field of wastewater treatment research.

2. Experimental

2.1. Materials

We utilized $Invitrogen^{TM}$ grade amidine-functionalized polystyrene (PS) latex particles obtained from Thermo Fisher Scientific, India, to prepare catalytically enabled rough particles for treating wastewater containing MB, model pollutant. The particle size specified by the manufacturer is 1.0 μm. However, the particle size determined through image analysis based on scanning electron microscopy (SEM) was 1.0 ±0.1 μm. An electrophoretic study was conducted to determine the particle's Zeta potential (ζ). The ζ potential of the PS particles in a 1 mM NaCl electrolyte medium was measured as 46 ± 3 mV. The Chloroplatinic acid hydrate, used as a precursor for nanoparticle synthesis and to deposit platinum (Pt) nanoparticles on the PS surface, was procured from Sigma-Aldrich Chemicals Pvt. Ltd., India. Sodium borohydride ($NaBH_4$), obtained from Sigma-Aldrich Chemicals Pvt. Ltd., was employed as a reducing agent. Hydrogen peroxide (30 w/v %), used in the decomposition reaction mixture to generate hydroxy radicals, was obtained from Thermo Fisher Scientific India, Pvt. Ltd. The model pollutant, MB, was procured from Sigma-Aldrich Chemicals Pvt. Ltd., India. All reagents received were of analytical grade and used without any further purification. All aqueous solutions experiments used deionized water from a Smart2Pure™ water purification system (Manufacturer: Thermo Fisher Scientific, Model: Smart2Pure 12 UV/UF).

2.2. Methods

2.2.1. Synthesis of Pt nanoparticles and rough particles

First, a stock solution of platinum precursor (H_2PtCl_6) was meticulously prepared in deionized (DI) water, maintaining a constant molarity of 10 mM. Subsequently, various molarities of 0.3, 0.5, 0.7, 1, and 1.3 mM solutions were prepared in different vials through dilution to determine the optimum one. A 10 mM concentration of sodium borohydride solution served as the reducing agent in the synthesis of platinum nanoparticles. A predetermined quantity of platinum precursor was combined with a tenfold excess volume of sodium borohydride solution in a designated beaker, ensuring thorough mixing at 140 rpm using a magnetic stirrer at room temperature. The mixture was left undisturbed for 4 h, during which time the transparent solution transitioned to a black hue, indicating completion of the reaction as shown in Fig. 1A. Following the reaction period, the formed nanoparticles were separated via centrifugation at 9500 rpm for 10 min. Subsequently, they were washed multiple times with water to eliminate any residual intermediate complexes in the suspension. The method reported by our group earlier was employed to synthesize the rough particles using Pt nanoparticles at a suitable precursor concentration [13]. The synthesis of PS/Pt rough particles involves mixing a known concentration of platinum precursor (1 mM) with PS particles (0.5 mg/mL) using a magnetic stirrer for up to 30 min. A reducing agent, sodium borohydride, is added to the mixture, followed by a 30 min equilibration period. The chemical reduction reaction is initiated by adding 5 mL of 10 mM sodium borohydride solution to the reaction mixture. To ensure maximum conversion, a ten-fold excess of sodium borohydride is used. After several centrifugation and washing cycles, the modified PS particles are subsequently separated from the supernatant.
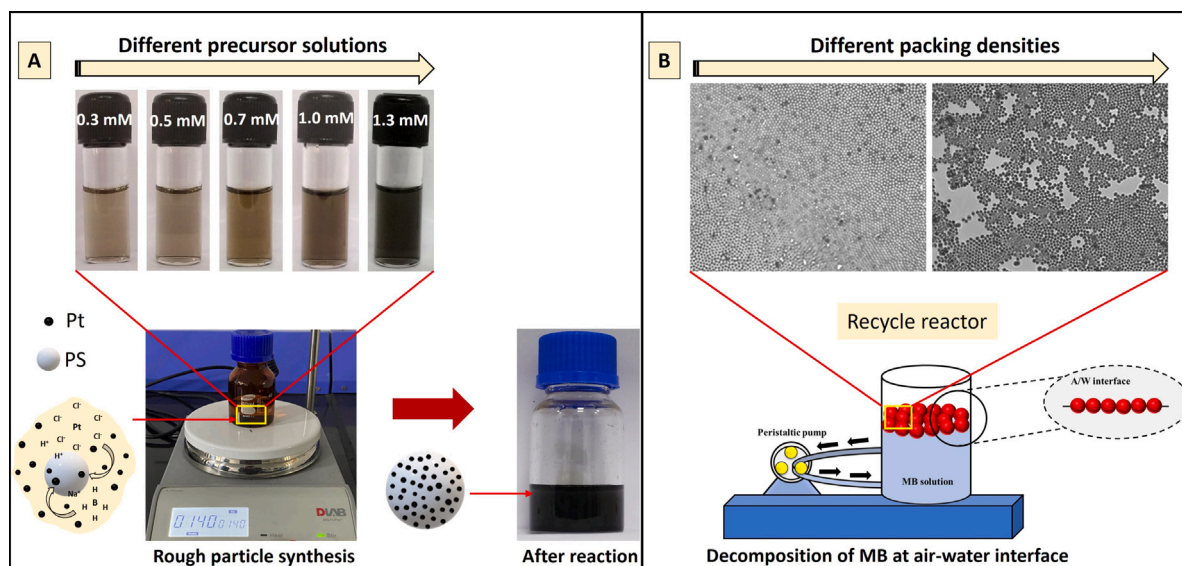
Fig. 1. Experimental insights: (A) Synthesis of platinum and PS-Pt rough particles at constant mixing at 140 rpm and at room temperature for 4 hr and (B) schematic description showing the decomposition of MB using rough particles at air–water interface.

2.2.2. Discoloration of MB using rough particles at air–water interface

A batch reactor is integrated with multiple input and output connections linked to the circulation pump, allowing for interchangeable assemblies using polymer tubes. The rough particles are deposited at the interface between air and the aqueous pollutant mixture. A peristaltic pump serving as the circulation pump for transporting the pollutant from top to bottom was employed to enhance the driving force, i.e., the concentration gradient, within the system, as shown in the schematic (Please refer to Fig. 1B). The inset shown in Fig. 1B corresponds to the microscopic images showing the monolayer assembly of rough particles at the air–water interface. In this way, the radicals generated by the decomposition of hydrogen peroxide near the interface are fed at the bottom through circulation so that the bulk pollutant starts to degrade continuously. On the other hand, the reactant molecules mixed with the radicals diffuse continuously from bottom to top due to displacement caused by circulation. As the recycle creates a marked difference in the mixing, one can observe the concentration gradients with an action of the peristaltic pump. Flow circulation is characterized by the Reynolds number, which can be calculated from the pump's RPM using the following equation [37]:

$$\omega = \frac{2\pi \times \text{RPM}}{60} \tag{1}$$

$$v = r \times \omega \tag{2}$$

$$Re = \frac{\rho \times v \times l}{\mu} \tag{3}$$

where, ω is angular velocity (rad/s), pump rotation (RPM), v is linear velocity (m/s), r is radius of the particle (m), water density (ρ) (kg/m^3), Water viscosity (μ) (Pa s), l is length of the pipe (m).

When circulation is maintained, forced diffusion occurs, where pollutants are actively transported throughout the treatment system due to mechanical agitation. This rapid movement enhances contact between pollutants and treatment agents, accelerating their breakdown. However, when circulation is halted, forced diffusion ceases, and molecular diffusion becomes the dominant mechanism. Molecular diffusion is a slower process driven by the random movement of molecules. Pollutants must rely on this slower motion to encounter treatment agents, leading to a delay in their degradation.

2.2.3. ANN methodology

In studying MB removal efficiency in water treatment processes, we employed Artificial Neural Networks (ANN) to address the inherent complexity that classical regression methods cannot adequately handle. ANN, a robust computational tool, is well-suited for analyzing intricate systems that defy description by conventional mathematical equations [38]. While non-linear models are frequently employed to optimize process parameters, ANN offers enhanced sensitivity in identifying the relationships between variables [39]. The artificial neural network (ANN) model comprises an input, hidden, and output layer, constituting a multilayer feedforward network architecture trained using the backpropagation algorithm [38]. The architecture consists of four input neurons representing time, stirring speed, MB concentration, hydrogen peroxide, and a single output neuron for predicting removal efficiency. We optimized the hidden layer by varying the number of neurons from 1 to 20 and tested several activation functions, including purelin, logsig, tansig, and ReLU. Given the limited dataset, the model architecture was configured with a single hidden layer and input and output layers. Additionally, optimizing the number of neurons in the hidden layer was crucial. This optimization was accomplished by systematically varying the neuron count within a predefined range, guided by an extensive review of the relevant literature. The experimental dataset, comprising time and removal efficiency data, was standardized to ensure equal contribution from all features. The dataset was divided into training (80%), validation (10%), and testing (10%) subsets, with early stopping employed to prevent overfitting. The early stopping mechanism monitored validation loss and restored the best model weights after a specified patience period. We evaluated the ANN with different numbers of neurons in the hidden layer to identify the optimal configuration based on Root Mean Square Error (RMSE). The best model configuration was selected based on the lowest RMSE. The Adam optimizer's learning rate was set to 0.001 during training to ensure effective convergence. Model performance was evaluated using RMSE, Mean Squared Error (MSE), and R-squared (R^2) values. The neuron function in the ANN model is defined as follows [40]:

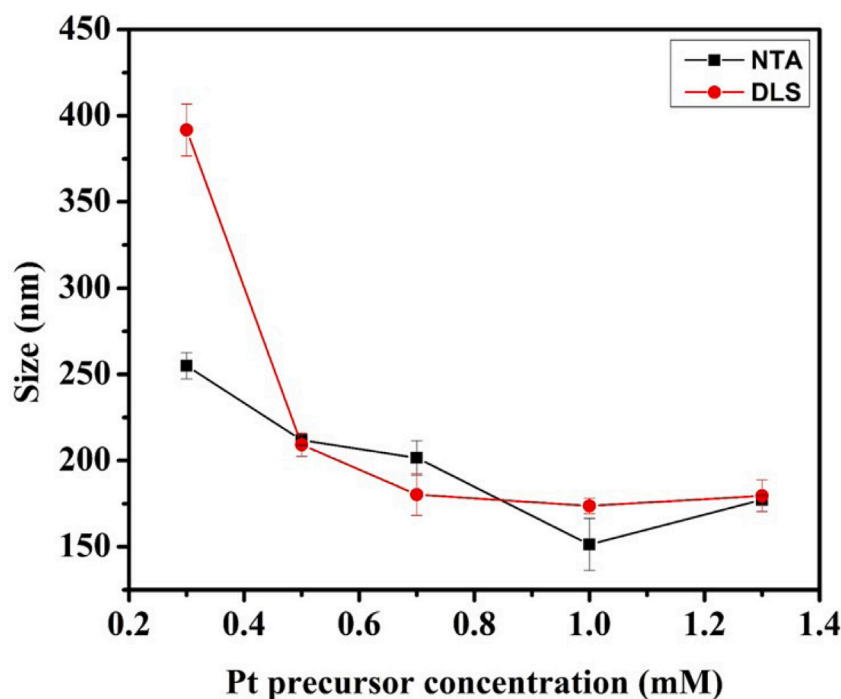$$y = \phi \left(\sum_{i=1}^{n} w_i x_i + b_i \right) \tag{4}$$

Fig. 2. Figure illustrates a comparison of the size difference in platinum nanoparticles with variations in platinum salt concentration.

where w represents the weights, b the biases, x the inputs, and Φ the activation function. The weights were adjusted iteratively using the backpropagation algorithm to minimize the error E, calculated by:

$$w_i \leftarrow w_i - \eta \frac{\partial E}{\partial w_i} \tag{5}$$

$$E = \frac{1}{n} \sum_{i=1}^{n} (y_i - \hat{y}_i)^2 \tag{6}$$

It is worth noting that the ANN modeling was performed using Python with the TensorFlow and Keras libraries. The resulting plots visualize the model's performance across different configurations, offering valuable insights into optimizing water treatment processes.

2.2.4. Characterization

The Zeta potential of bare polystyrene (PS) and rough PS particles was measured using a Zetasizer obtained from Malvern Panalytical (Model: ZSP), employing the electrophoretic light scattering (ELS) technique. The average diameter of 1.0 μm PS particles was determined using a Field-emission scanning electron microscope (FESEM) from FEI, USA (Model: Inspect F). Additionally, the hydrodynamic diameter of the 1 μm PS particles and platinum (Pt) particles was determined using a dynamic light scattering technique (Make: Malvern Panalytical, Model: ZSP) and Nanoparticle Tracking Analysis (NTA), Make: Malvern Panalytical, Model: NS300. To confirm the distribution and size of the nanoparticles on the as-synthesized rough particles engineered with Pt, the electron mapping analysis using a scanning electron microscope from JEOL Ltd., Japan (Model: JSM-6610) and atomic force microscopy (AFM), Bruker Corporation, Germany; Model: Multimode-8 AFM were employed, respectively. The surface morphology of PS rough particles was captured using an inverted microscope (Make: Leica microsystems, Model: DM IL LED Fluo). X-ray diffraction (XRD) (make: Bruker Corporation, Germany, model: Bruker D8 Venture) was employed to investigate the structural properties of both polystyrene (PS) particles and platinum-coated PS rough particles in their original synthesized form. Furthermore, the kinetics study of the chemical decomposition of MB was investigated by monitoring concentration as a function of time using a UV–VIS spectrophotometer obtained from Thermo Fisher Scientific, India (model: GENESYS 10S UV–Vis).

3. Results and discussion

3.1. Characterization of Pt and rough particles

The hydrodynamic diameter of the synthesized Pt nanoparticles was measured using DLS and NTA at various precursor concentrations by dispersing them in water at appropriate amounts (0.01 w/v %) to prevent aggregation in the suspension. The particles were suspended in a 1 mM NaCl solution for zeta potential measurements. It was observed that increasing the precursor concentration led to the formation of smaller nanoparticles, as illustrated in Fig. 2. Specifically, nanoparticles with a size of 150 nm were formed at a precursor concentration of 1 mM. However, further increases in concentration resulted in larger nanoparticle sizes, likely due to particle aggregation, as detected using NTA. Results obtained from DLS also exhibited a similar trend, although the measured sizes were slightly higher. DLS data indicated that the particle size remained relatively constant after reaching a precursor concentration of 0.7 mM. Subsequent increases in precursor concentration did not significantly affect the particle size. As previously reported, these findings align well with the mean aggregate size deduced from DLS [41]. The tendency of metallic nanoparticles to aggregate stems from their surface properties, characterized by strong van der Waals force. Atomic Force Microscopy (AFM) and Transmission Electron Microscopy (TEM) were also employed to study the nucleating particle size or the monomeric unit of Pt nanoparticles, which are the building blocks of nanoparticle aggregates. Atomic Force Microscopy (AFM) and Transmission Electron Microscopy (TEM) were used to analyze the nucleating particle size or monomeric unit of Pt nanoparticles, which are the building blocks of nanoparticle aggregates. The particles were spread on a silicon wafer using the drop-casting technique. A 0.01 w/v % concentration of particles diluted in DI water was used for these analyses. The samples were dried in a forced air oven at 80 °C overnight (12 h).

Figs. 3 A-D show the surface morphology and size distribution plot obtained from analyzing TEM and AFM images. These images reveal that the particles are poly-disperse, and the average size of the nanoparticles varies from 15 to 40 nm with a mean particle size of 25 nm. It is worth noting that 100 representative particles were
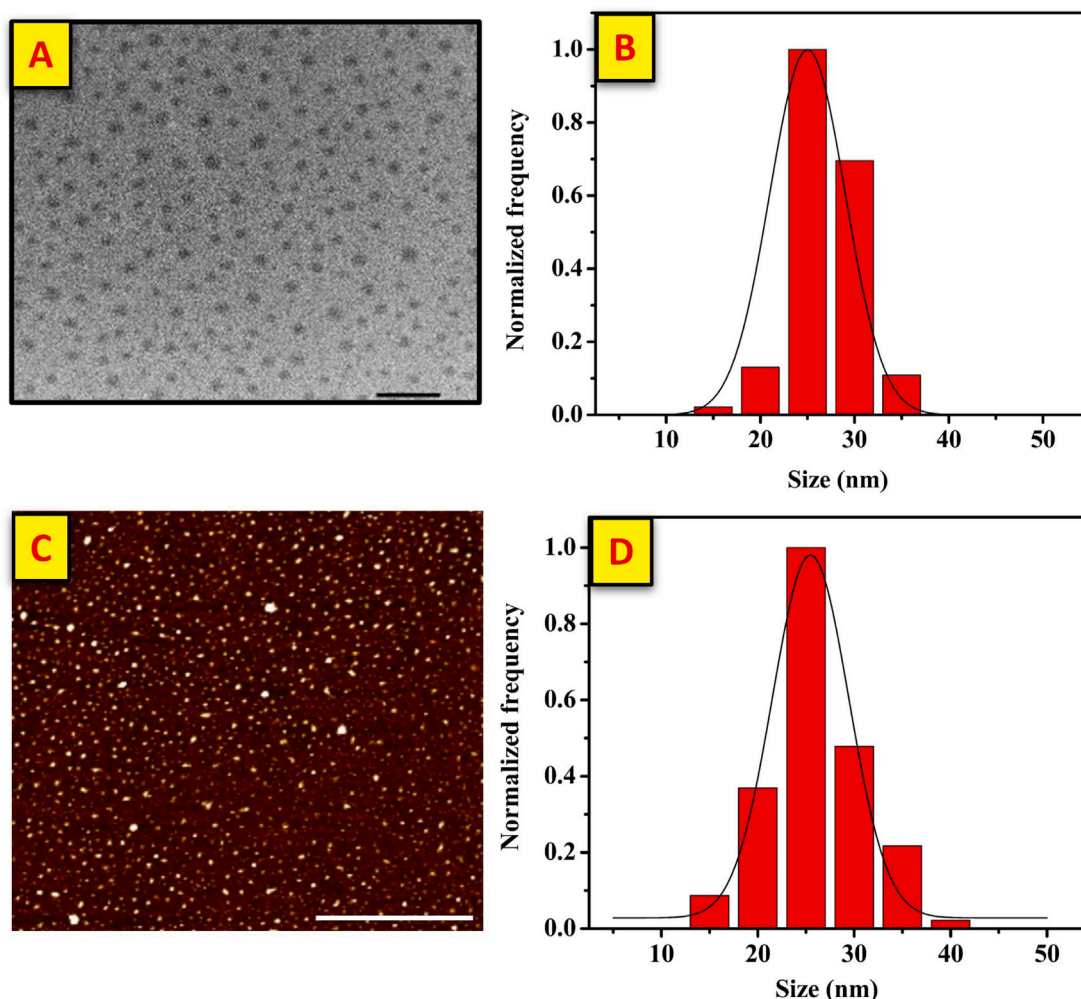
Fig. 3. Microscopic insights: (A) TEM morphology and (B) size distribution of the Pt-nanoparticles. The scale bar given in the TEM image corresponds to 200 nm. (C) AFM morphology and (D) size distribution of the Pt-nanoparticles. The scale bar given in the AFM image corresponds to 1000 nm.

considered for the image analysis using imageJ to obtain the size distribution plot. The analysis was performed by diluting and drop-casting on a suitable substrate, which resulted in well-dispersed nanoparticles upon visualization under AFM and TEM. The findings from Figs. 2 and 3 help us understand the variation in nanoparticle size depending on their state, whether well-dispersed (TEM/AFM) or aggregate (DLS/NTA). Fig. 4 A-C presents the morphological characteristics of the PS/Pt particles alongside electron mapping, illustrating the uniform distribution of platinum nanoparticles on the PS surface at a reaction time of 4 h and precursor concentration of 1 mM. However, Fig. 4D-F presents the Atomic Force Microscopy (AFM) analysis and corresponding line cut analyses, elucidating the deposition of platinum particles on the surface of polystyrene (PS). This examination offers a detailed insight into the topographical features, revealing distinct surface roughness patterns indicative of the formation of rough particles. The clarity of the images provides compelling evidence regarding the distribution and arrangement of platinum particles on the PS substrate, facilitating a comprehensive understanding of the deposition process. Observation of Fig. 4 suggests that the rugged PS particles are adorned with Pt nanoparticles, akin to speckles adorning the skin with white spots. It can be inferred from Figs. 3 and 4 that the dispersed state of the nanoparticles resembles the islands-like morphology. Fig. 5 depicts the X-ray diffraction (XRD) pattern acquired from the particles under examination. Analysis revealed that the characteristic peaks observed at 39.81° and 46.31° correspond to the crystallographic

orientations of 110 and 200, respectively, confirming the presence of platinum nanoparticles. These observations corroborate with findings documented in prior literature, reinforcing the consistency and validity of the reported results [41]. It comes to say that the application of rough particles synthesized by immobilizing the Pt nanoparticles on the surface of PS particles offers enhanced exposure and catalytic efficiency compared to pristine Pt nanoparticles, owing to their reduced tendency to aggregate. Furthermore, the detailed XRD and FESEM analysis conducted after five degradation cycles confirm the structural and compositional integrity of the catalyst, showing no signs of degradation even after repeated use.

Using rough particles embedded with Pt nanoparticles has opened up new possibilities for treating wastewater containing specific pollutants. Building upon previous work by our group [13], which focused on the chemical decomposition of MB dye and tetracycline pharmaceutical residues, significant progress has been made in identifying optimal parameters such as contacting patterns, particle size, concentration, and reagent dosing volume. While the cost factor is mitigated by employing magnetically responsive rough particles (MR-RP), scaling up and recycling the particles after each use is a persistent challenge. Our current strategy aims to achieve a suitable trade-off between time and particle concentration at the air–water interface rather than in the bulk solution. This technique attempts to enhance particle use efficiency and enhance overall process sustainability.
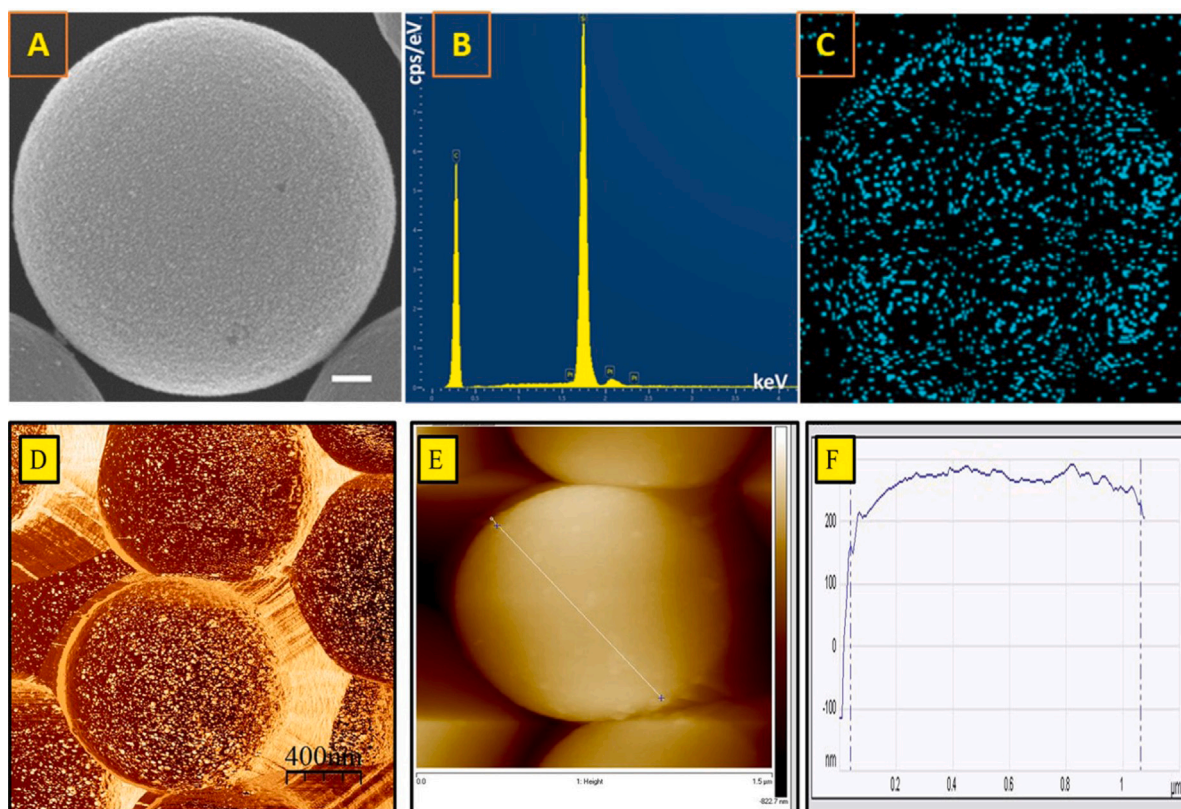
Fig. 4. The surface characterization of rough particles. (A) FESEM, (B) EDS analysis to confirm the presence of Pt, and (C) electron mapping, depicting the islands-like morphology of platinum nanoparticles distributed uniformly on the surface of the micron-sized polystyrene particles. (D-F) AFM images corresponding to the surface morphology (D) and the line cut analysis (E and F). The scale bar given in the FESEM image (A) corresponds to 100 nm.
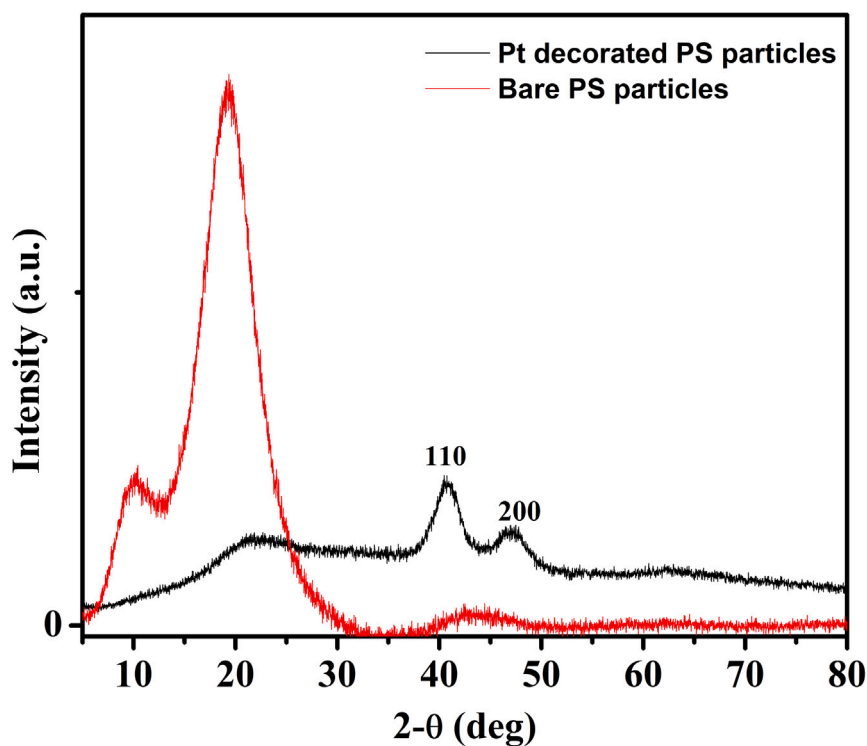

Fig. 5. XRD analysis confirms the presence of platinum (Pt) on the surface of 1 μM polystyrene (PS) particles.
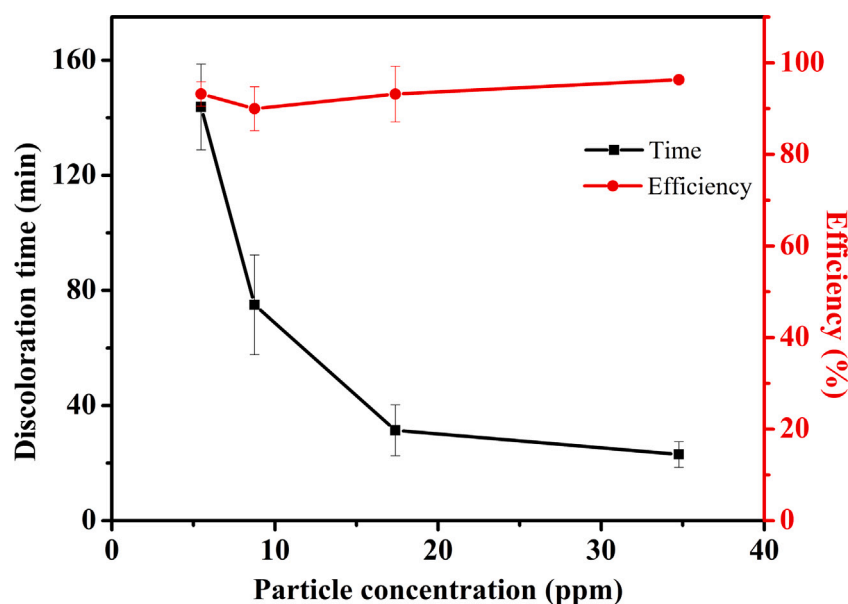
Fig. 6. A quick insight into the chemical decomposition of MB showing discoloration time and catalytic efficiency as a function of the concentration of rough particles through the bulk approach. The initial concentration of MB maintained throughout is 10 μM.

3.2. Discoloration of MB at air–water interface

First, we share an analogy proposed by our group regarding bulk phenomena before discussing the interface approach [13]. Fig. 6 shows that increasing the concentration of rough particles in the bulk results in better removal efficiency and a shorter time to eradicate MB species. However, the bulk approach is costly due to the amount of catalyst particles involved. One can trap the particles at the air–water interface to degrade MB entirely instead of dispersing them in bulk. However, this may result in a longer decomposition time as it is inversely proportional to the concentration. Combining the interface approach with a circulation of the reaction mixture can significantly reduce the reaction time by many folds, the result of which is discussed in the subsequent sections. It can be noticed that the efficiency of the catalytic-assisted reaction considered for the analysis is more or less the same, although varying slightly between 91 and 96%.

The proposed method, illustrated in Fig. 1B, capitalizes on rough particles deposited at the interface to initiate chemical decomposition directly at the contact point. Catalytic activity from hydrogen peroxide generates radicals, which help break down the target pollutants. This approach establishes two distinct zones: treated and untreated. Controlling the movement of the boundary between these zones is crucial for managing chemical reactions effectively. The peristaltic pump, depicted in Fig. 1B, promotes mixing and re-circulation, swiftly transporting fresh pollutants from the bulk to depleted phases. Fig. 1B shows the schematic of the dye degradation, with the inset displaying the particle arrangement at the A/W interface. For more information on the experimental setup, please refer to the details in the Experimental section. In short, we established an interface between air and water to degrade the industrial model dye, MB. The physicochemical kinetics of the rough particles were recorded by trapping them at the interface with a packing fraction ranging from 0.5 to 0.8. Thus, one can readily control the discoloration time scales by adjusting the packing fraction as the number of rough particles deposited at the interface varies for a reactor diameter of 0.063 m. In the water phase, there was a homogeneous solution of MB (total volume 200 mL, MB concentration 10 μM or 3.2 PPM) in a reactor with circulation. The circulation of the pollutant is further facilitated using a peristaltic pump set at 50 rpm, circulating from top to bottom to ensure equilibrium and minimize concentration gradients within the water phase. In this way, several studies were conducted by manipulating the circulation speed from

10 to 50 rpm at a 0.8 packing fraction to investigate its effect on degradation further.

3.3. The effect of circulation speed on MB degradation

The breakdown of MB relies on the catalytic reaction of H_2O_2 at the particle interface, which accelerates pollutant degradation through rapid contact. It takes about 9 h for MB to break down in still conditions (without circulation), as demonstrated by the reactor's clear phase zone length over time (Please refer to Fig. 7A). However, complete decomposition occurs within $\approx$ 30 min when circulation is activated and optimized. Fig. 7B illustrates the effect of circulation on the formation of the concentration gradient during MB degradation. The circulation of the pollutant from top to bottom reduces the concentration gradient by continuously transporting OH^- radicals to the bottom and enhancing the contact mixing between non-degraded MB molecules and the particle interface. This process increases the multi-fold contact time between rough particles and MB, replacing old fluid with fresh fluid via circulation. It is important to note that all air–water interface MB decomposition trials utilized 200 mL of pollutant (MB) at a concentration of 10 μM and 5 vol% of H_2O_2 per batch. It is also important to note that increased circulation speed reduces reaction time, breaks up the particle monolayer, or moves particles towards the wall. Therefore, an intermediate circulation speed is necessary for effective degradation, and circulation beyond 50 RPM is not preferable for the studies (Please refer to Fig. 8A). Through optimization, we have determined that a circulation speed of 50 RPM is optimal for achieving complete MB degradation within a minimal time frame. At speed < 50 RPM, the circulation effectively prevents gradient formation while avoiding monolayer detachment.

3.4. Effect of packing fraction (Φ) on the MB degradation

The packing fraction of particles at the interface plays a crucial role in the degradation of pollutants, as a greater surface area facilitates the rapid conversion of H_2O_2 and decomposition of MB. We optimized the Φ using different number densities of the rough particles ranging from a closely-packed arrangement to a loosely-packed arrangement while keeping the concentrations of hydrogen peroxide (5 w/v %) and pollutant (10 μM) constant, along with an optimum circulation speed
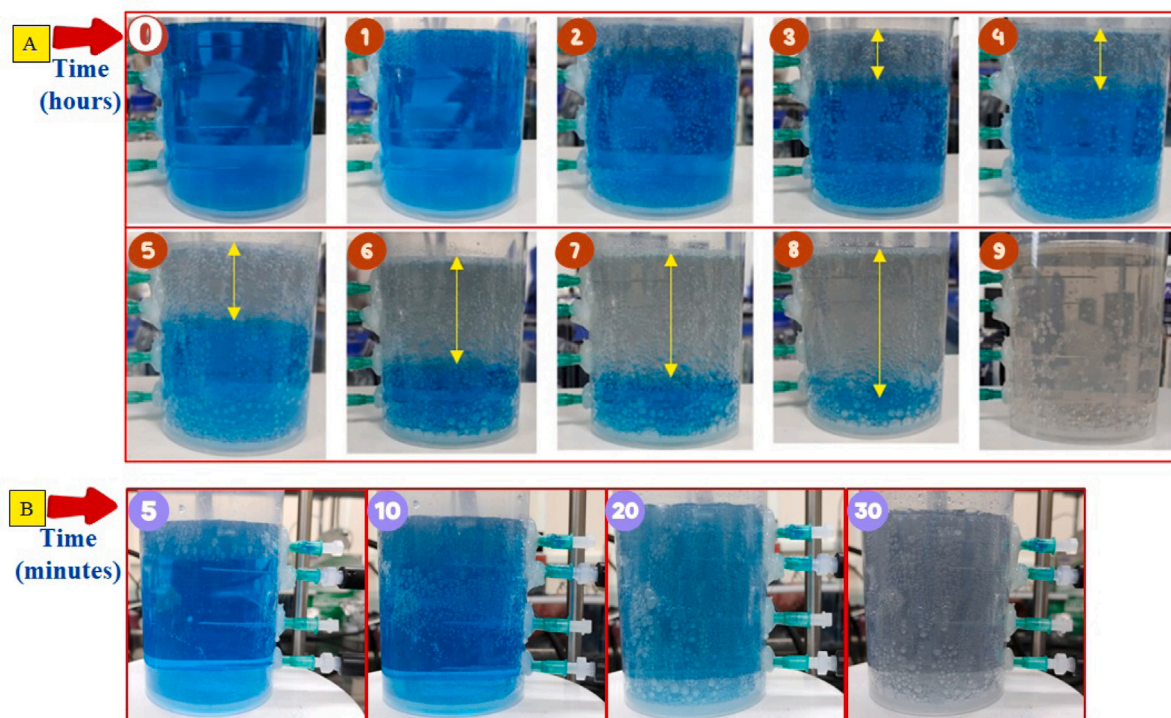
Fig. 7. (A) Photographs depicting the formation of the concentration gradient during the degradation of MB without circulation. (B) Photographs depicting the absence of concentration gradient formation with a circulation speed of 50 RPM and the complete degradation of MB within 30 min.
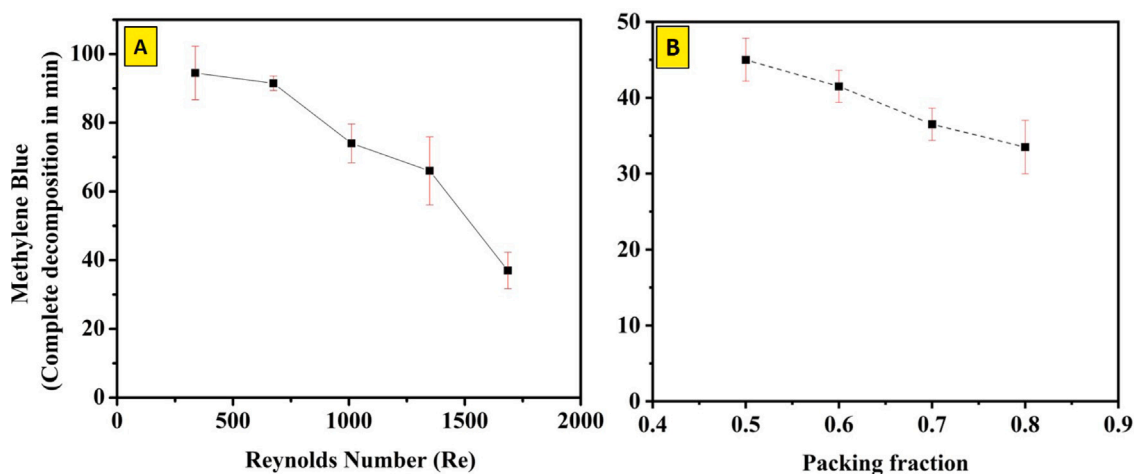

Fig. 8. Plot showing the decomposition of MB. (A) At different circulation speeds and fixed Φ = 0.8. (B) At different packing fractions and fixed NR_e = 1686.

of 50 rpm (NR_e = 1686). This approach demonstrated the effect of Φ at the interface on pollutant degradation. The close examination of Fig. 8B suggests that the degradation time is inversely proportional to the Φ, indicating that a decrease in the Φ at the interface results in less surface area exposed to H_2O_2 and slower decomposition, leading to a longer degradation time of the pollutant. Fig. 9 demonstrates the representative microscopic images depicting the packing of particles at the A/W interface before and after degradation, clearly indicating the changes in the packing densities.

We conducted a separate study to determine the optimal conditions to minimize the packing losses while maximizing the decomposition of hydrogen peroxide (H_2O_2). It is important to note that the oxygen produced due to the decomposition of H_2O_2 is released into the water phase as bubbles rise to the surface. The collapse of these bubbles at the interface signifies a substantial reduction in the packing density. To curb this issue and assess its impact on the catalytic concentration, the

desired % volume of H_2O_2 at the optimized condition of Φ = 0.5% was used at the air–water interface. The representative microscopic images captured before and after the degradation experiments were utilized to deduce % change in packing densities during the pollutant degradation. The % change in packing densities can be defined as follows:

$$\%change = \frac{\Phi_i - \Phi_f}{\Phi_i} \tag{7}$$

Where Φ_i and Φ_f refer to packing densities corresponding to initial and final configurations, respectively. The information about the Φ was deduced using imageJ, an image processing tool.

Fig. 10 illustrates the percentage losses in packing fraction concerning H_2O_2 concentration. The packing losses remain minimal until reaching 1.5 vol% of H_2O_2. Beyond this concentration, there is an increase in losses within the system. However, employing this concentration would excessively prolong the degradation of pollutants.
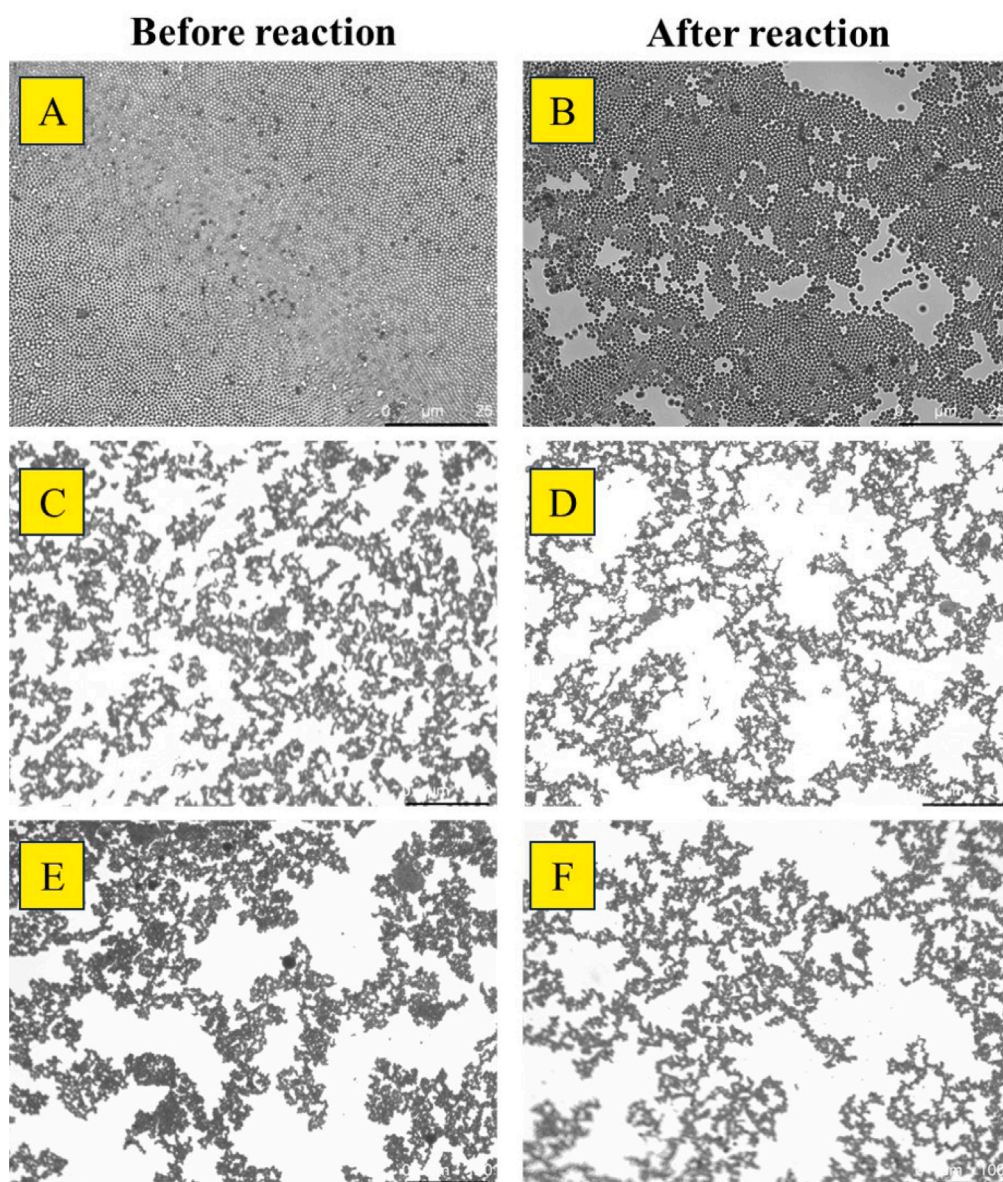
Fig. 9. Figures A and B depict the condition of 0.8 packing before and after MB degradation, respectively, at a 5% H_2O_2 concentration. Figures C and D show the condition of 0.5 packing before and after MB degradation, respectively, at a 1.5% H_2O_2 concentration. Figures E and F illustrate the condition of 0.5 packing before and after MB degradation, respectively, at a 3% H_2O_2 concentration. The scale bar on A-B, C-D, and E-F correspond to 25, 100 and 100 μm, respectively.

Nevertheless, at 3 vol% H_2O_2, the losses remain nominal (< 10%) under optimized conditions. Therefore, one can utilize 3 vol% as the working concentration for pollutant degradation within the effective time interval.

4. Degradation kinetics

The kinetics concerning the degradation of MB over time have been studied using a UV-visible spectrometer. The degradation mechanism of MB follows the pseudo-first-order Langmuir–Hinshelwood (LH) kinetics, as described by our group earlier [13]. The MB absorbance was observed at 664 nm (Please refer to Fig. 11 for the details on the UV-vis characteristics of MB). Fig. 12 A shows the MB decomposition over time under optimum conditions: 3% H_2O_2, a packing factor 0.5, and a circulation at 50 rpm. The system achieved complete pollutant degradation, with a concentration of ≈ 10 μM in a 200 ml batch, within 140 min. Besides efficiency, determining the reaction order and rate constant provides The kinetics of heterogeneous catalytic processes that

can be described using the Langmuir–Hinshelwood (LH) kinetics model, as shown in Eq. (8) below [13],

$$r = -\frac{dC}{dt} = \frac{k_r KC}{1 + KC} \tag{8}$$

Where r, k_r, K, and C represent the reaction rate, the limiting rate constant of reaction at maximum coverage under the given experimental conditions, the equilibrium constant, and the concentration at any time t during degradation, respectively.

The literature has demonstrated that Eq. (8) follows first-order kinetics, i.e. $n = 1$, by assuming KC≪1. Thus, when $-ln(\frac{C}{C_0})$ is plotted on the ordinate and time is plotted on the horizontal axis, the slope of the straight line corresponds to the product of k_r and K. However, if the slope value found is ≫ 1, the assumption that KC≪ 1 becomes invalid, indicating that subsequent kinetics will be in zero order. Fig. 12 B shows the decomposition kinetics of the MB as a function of time. As the Y regression on X yields a straight line, it can be asserted that the decomposition characteristics obey the first-order kinetics corresponding to the heterogeneous reactions catalyzed
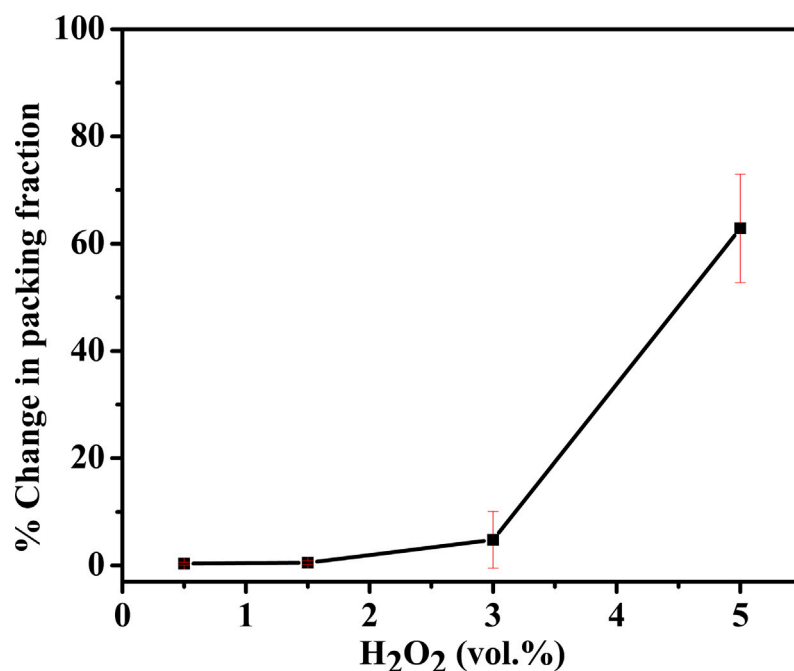
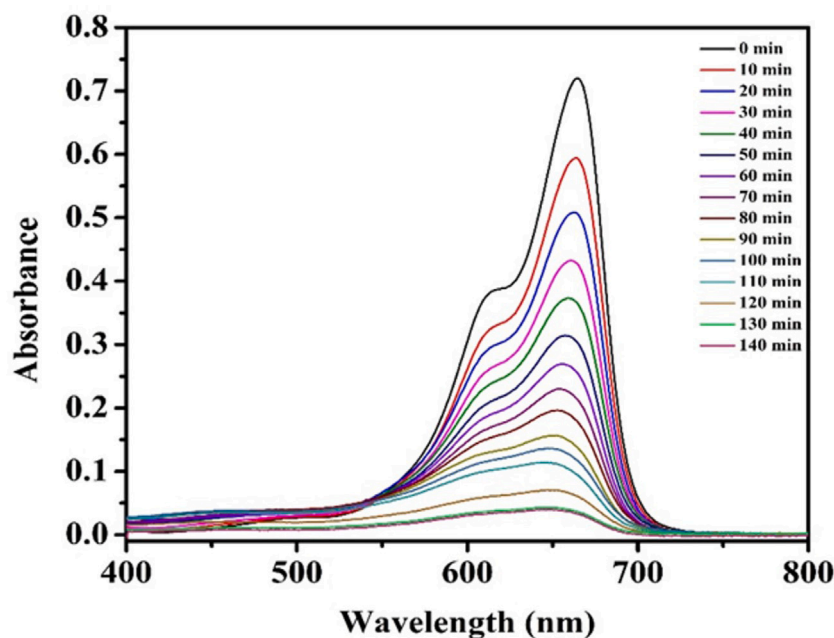**Fig. 10.** Plot depicting the % change in the packing fraction as a function of hydrogen peroxide concentration.

Fig. 11. The plot showing the absorbance spectra corresponding to the decomposition of MB over time ($\Phi = 0.5$, $H_2O_2 = 3\%$, circulation speed = 50 RPM.).

by the rough particles. The kinetics presented achieved a linear fit up to 110 min, i.e., removal efficiency = 86.4%, yielding the rate constant of 0.018 min^{-1} for the reaction promoted by 1 μm rough particles. These L-H kinetic studies agree with the MB degradation catalyzed by rough particles, as described by our group earlier [13]. Beyond 110 min, however, the kinetic profile observes a deviation from linearity. The observed deviation may result from several factors, including mass transfer limitations at lower dye concentrations and the gradual depletion of H_2O_2, which is the primary source of hydroxyl radicals in the system. As the H_2O_2 concentration diminishes over time without replenishment, fewer reactive radicals are produced, reducing the oxidative capacity and slowing the reaction rate. Consequently, the degradation process slows down because it becomes limited by

the availability of reactive species or the rate at which they reach the catalyst surface. These combined effects account for the observed slowdown in the degradation rate after 110 min.

5. ANN modeling of MB removal

The architecture of the ANN model used in this study is depicted in Fig. 13A. This study focused on the impact of multiple independent variables on the removal efficiency of MB. Thus, the neural network's input layer was designed with four neurons. As the objective of the neural network was to perform a regression task, the output layer comprised only one neuron representing the predicted removal efficiency. The number of neurons in the hidden layer varied from 1 to
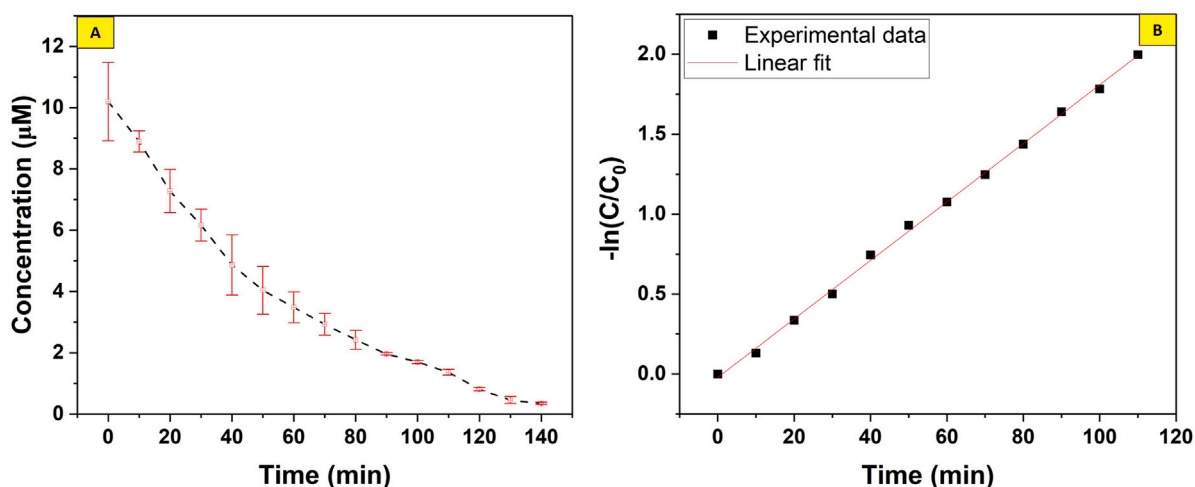
Fig. 12. Plot showing the (A) concentration vs time and (B) kinetics of the MB decomposition obtained from absorbance spectra at optimized conditions, i.e., Φ = 0.5, H_2O_2 = 3%, circulation speed = 50 RPM.
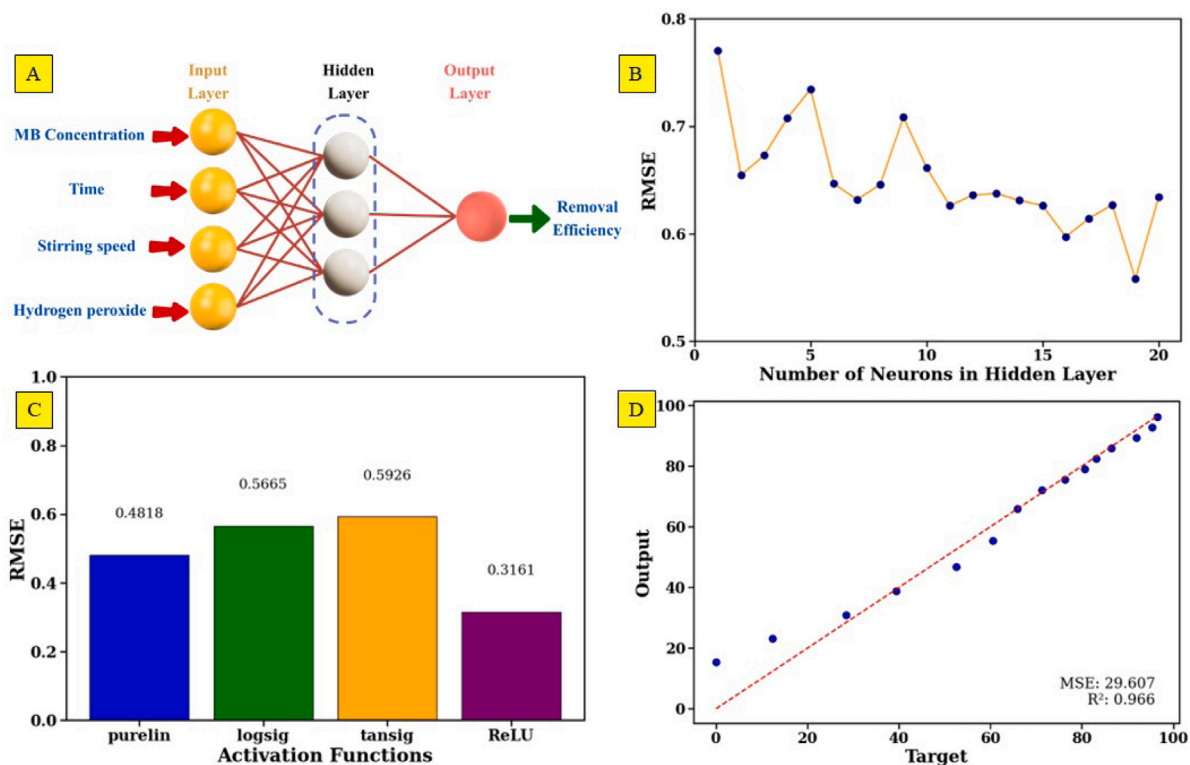

Fig. 13. (A) Architecture of the ANN model (4-19-1) with input features including Time, MB Concentration, Speed, and Hydrogen Peroxide. (B) RMSE values corresponding to different numbers of neurons in the hidden layer, with the optimal number of neurons identified. (C) RMSE values for different activation functions (purelin, logsig, tansig, ReLU) demonstrating the performance of each. (D) Comparison of actual and predicted values for the MB removal efficiency, showcasing the model's predictive accuracy.

20, and the resulting Root Mean Square Error (RMSE) values were recorded (Fig. 13B). The optimal model for predicting MB removal was achieved with the minimum RMSE value of 0.5580, using 19 neurons in the hidden layer. This configuration was used for subsequent analyses. Furthermore, the performance indicator (RMSE) was computed for various activation functions, specifically purelin, logsig, tansig, and ReLU, as illustrated in Fig. 13C. Among the evaluated activation functions, the ReLU function demonstrated the highest efficiency for the optimal neural network, with an RMSE value of 0.3161. Throughout the training process, the model with the highest R^2 value and lowest RMSE value served as the primary criterion for determining

the stopping point of the training. The ANN model's performance was examined using metrics such as Mean Squared Error (MSE), RMSE, and R^2 values. The optimized ANN model established a favorable correlation with the training data, as depicted in Fig. 14A. It also demonstrated relatively good performance in validation and testing datasets, as shown in Figs. 14B and 14C, respectively. The strong correlation demonstrated in the data confirms the strong generalization capability of the ANN model, which effectively minimizes the risk of overfitting. The training process involved an early stopping mechanism to enhance further model robustness, which monitored validation loss to prevent overfitting and attain optimal convergence. Additionally, the
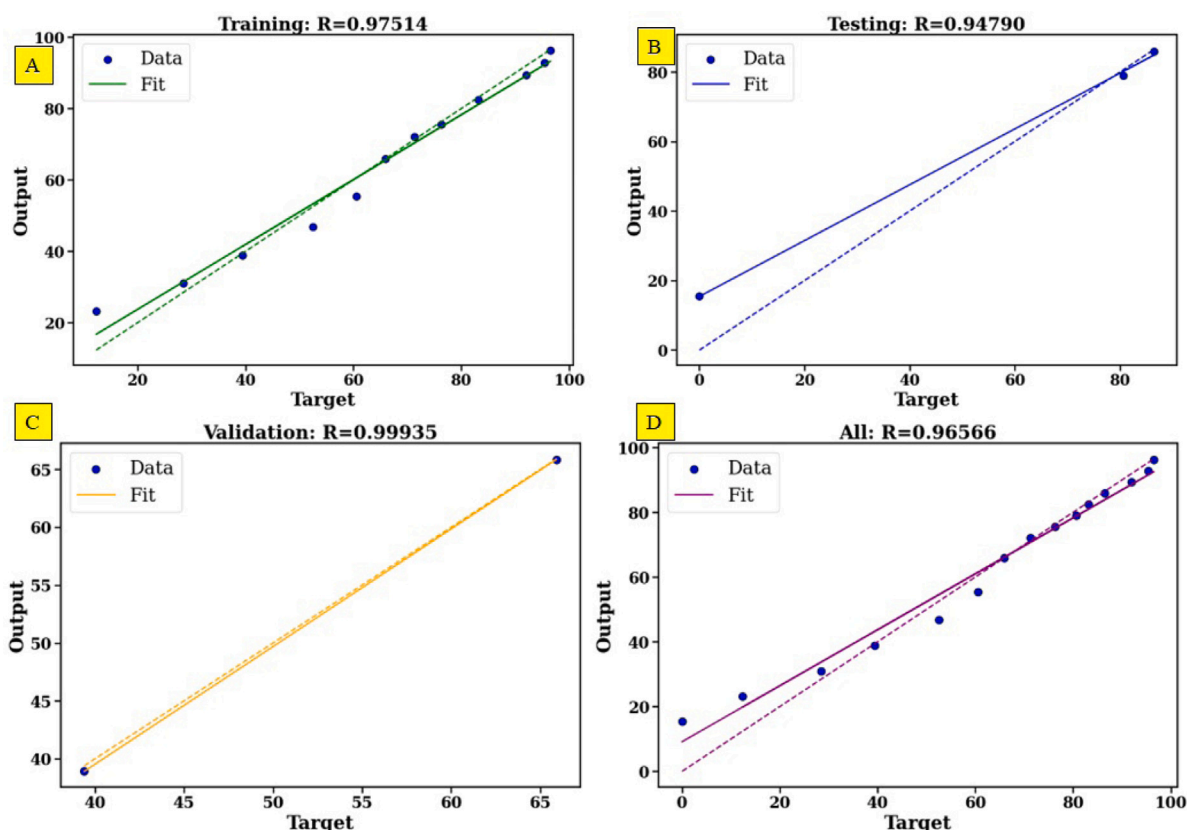
Fig. 14. (A) Training data showing the correlation between actual and predicted values. (B) Testing data illustrating the accuracy of the model predictions against actual values.(C) Validation data depicting the model's performance in predicting unseen data.(D) Combined data representing the overall fit between actual and predicted values across the entire dataset.

dataset was randomly shuffled before splitting, and model training was repeated using multiple random seeds, all of which yielded consistent performance, confirming the model's robustness. The model's R^2 value of 0.9656 across the entire dataset range verifies its success in accurately modeling the complex nonlinear interactions among the most significant input parameters, including MB concentration, hydrogen peroxide dose, and removal efficiency. Overall, the performance of the ANN model was satisfactory for the experimental dataset, with an R^2 value of 0.9656 (Fig. 14D). Additionally, the Mean Absolute Error (MAE) for the optimized ANN model was calculated to be 4.3, further validating its predictive accuracy. Considering that the MB removal efficiency ranges between 0% and 100%, this relatively low MAE indicates a high level of predictive accuracy and underscores the model's capability to generalize across diverse experimental conditions reliably. To further validate the ANN model, we compared its predictive performance with the Langmuir–Hinshelwood (L-H) kinetic model traditionally used to describe heterogeneous catalytic reactions as illustrated in Fig. 15. The comparison showed that while both models provided satisfactory results, the ANN model displayed greater flexibility in handling the system's nonlinearities and incorporating multiple variables simultaneously. This capability allowed the ANN to outperform the L-H model regarding predictive accuracy, especially when dealing with a broader range of experimental conditions. The ANN model has proven effective in capturing the complexities of MB removal dynamics by demonstrating strong predictive capability across multiple datasets and conditions. Fig. 14D compares the predicted removal efficiencies against the experimental values using the best-performing ANN model (optimal number of neurons and ReLU activation function). The scatter plot demonstrates a strong correlation between predicted and actual values, with points closely aligning along the diagonal line, indicating high model accuracy and generalization capability.

Additionally, Fig. 13D assesses the model's performance, showing that the predicted outcomes of the ANN model closely matched the actual values, with a Root Mean Squared Errors (RMSE) value of 5.5. This result indicates that the ANN-based model can predict the removal efficiency of MB through the water treatment process.

Table 1 presents the performance of various catalysts in decontaminating wastewater containing MB, assessed using the catalyst-to-MB ratio metric 'M'. The table allows for assessing the materials' effectiveness, with lower 'M' values indicating greater catalyst performance. It is worth noting that, excluding rows 2 (M = 33.3), 3 (M = 33.3), and 11 (M = 100), the remaining results generally show similar performance when compared to each other. Among the reported studies, Hsieh et al. [21] demonstrate the highest performance with 'M' = 1.0. While slightly higher with 'M' = 1.5, our method achieves a similar removal efficiency of approximately 86.4% within 110 min of reaction time, indicating comparable performance. These findings underscore the promising potential of our approach, particularly with rough particles, suggesting significant avenues for further enhancement. Unlike the work of Hsieh et al. [21], it is worth noting that our proposed method works at room temperature.

6. Future scope and limitations

The proposed method leverages the catalytic particles to deactivate the target pollutant present in the sub-phase. Hence, the novelty of the method lies in its ability to extend the application to the oil-water interface to perform the decontamination in superphase. For instance, it can effectively eliminate water-soluble and oil-soluble dyes such as MB and solvent blue 4 (1-Naphthalenemethanol) in a single step. Further, since the reactor is configured with re-circulation from top to bottom to improve mass transfer and chemical kinetics, the proposed
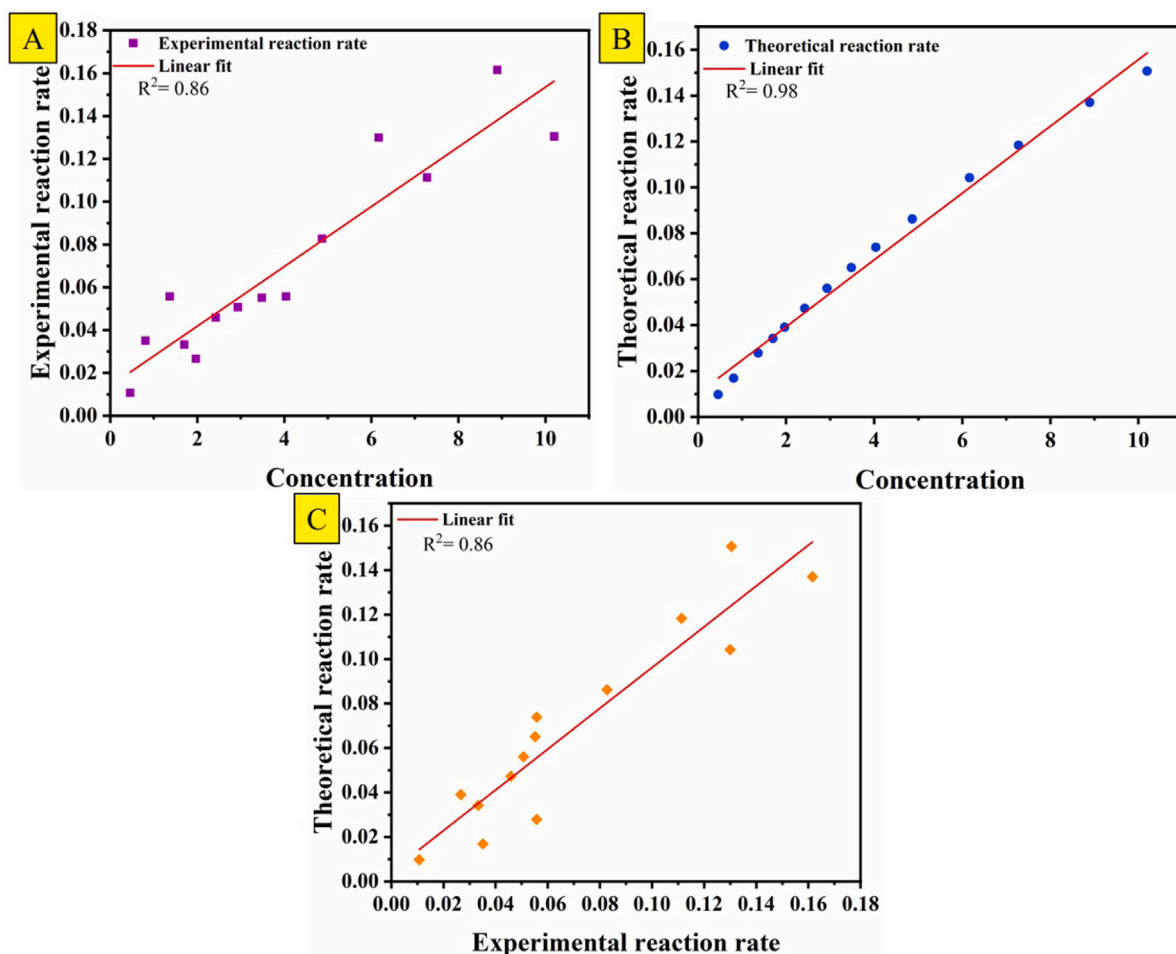
Fig. 15. Figure shows the Langmuir–Hinshelwood (L-H) kinetic model, with experimental and theoretical reaction rates plotted against concentration (A, B) and between each other (C), demonstrating a good fit with R^2 values ranging from 0.86 to 0.98.

Table 1

Comparison of the various techniques.

Materials	Catalyst	Contaminant	M = Catalyst/MB ratio	Removal efficiency(%)	Time (min)	Reference
Fe_3	PCN-250 (500 PPM)	MB (15 PPM)	33.3	88	720	Kirchon et al. [42]
Fe_3Mn	PCN-250 (500 PPM)	MB (15 PPM)	33.3	100	720	Kirchon et al. [42]
MIL-100	(1000 PPM)	MB (500 PPM)	2.0	42	230	Lv et al. [43]
Fe	MIL-100 (1000 PPM)	MB (500 PPM)	2.0	94	230	Lv et al. [43]
Fe_2O_3	(1000 PPM)	MB (500 PPM)	2.0	59	230	Lv et al. [43]
MIL-100	(1000 PPM)	MB (500 PPM)	2.0	95	230	Lv et al. [43]
Fe	MIL-100 (1000 PPM)	MB (500 PPM)	2.0	85	230	Lv et al. [43]
Fe_2O_3	(1000 PPM)	MB (500 PPM)	2.0	61	230	Lv et al. [43]
Fe-Pt	Fe-Pt (5 ppm)	MB (5 ppm)	1.0	90	90	Hsieh et al. [21]
Fe_3O_4	(500 ppm)	MB (5 ppm)	100	55	90	Hsieh et al. [21]
PS-Pt	Pt (5 PPM)	MB (3.2 ppm)	1.5	86	110	This study

setup can mimic the recycle reactor, wherein the product is fed back into the reactor. However, the difference, in this case, will be the direction of the reaction, which proceeds from the interface to bulk compared to the conventional reactors. The proposed method is not a good alternative if the catalytic-assisted reaction is carried out at the interface instead of bulk without circulation. Yet, with controlled circulation, it offers a suitable alternative to conventional methods. Even under optimum conditions, the performance of the interfacial recycle reactor outnumbers the bulk method slightly, i.e., discoloration time = 143 min, which is a significant advantage. On the contrary, it is possible to increase the catalytic loading in bulk depending on the initial concentration of the pollutant. In contrast, the proposed method is hindered by the limitation set by the interfacial area, which is a significant setback. Nonetheless, unlike conventional approaches,

it confines rough particles to the interface, eliminating the need for additional steps like separation and reuse cycles.

7. Conclusion

The study outlines the parameter optimization for synthesizing platinum nanoparticles using various characterization techniques. The study successfully synthesized Pt/PS rough particles using a single-step approach under optimal conditions. Additionally, the study explores the potential of utilizing platinum-studded PS particles at the air–water interface. The effects of circulation and different packing arrangements of these studded particles were examined. The findings exhibit critical data on rough particle catalytic activity at the air–water interface for

decontaminating wastewater with a target pollutant. This study elucidates the intricate relationships between pollutants and nanoparticles, enhancing understanding of their role in catalytic efficiency through meticulous analysis of such parameters as circulation velocity and packing structure. Interestingly, the rough particles deposited at the air–water interface achieve complete decomposition within approximately 30 min when the circulation is activated at a programmed speed of 50 RPM (NR_e = 1686). This response is very significant when compared to 9 h under still conditions. Furthermore, the interface approach under optimum conditions provides an equal or slightly more improved performance than the bulk approach. The predictive performance of an artificial intelligence-based model employing an artificial neural network (ANN) approach was evaluated to validate the experimental findings on the removal efficiency of MB. The ANN model demonstrated exceptional predictive capability, achieving a low root mean squared error (RMSE) of 5.5 and a high coefficient of determination (R^2) value of 0.9656, indicating a high degree of accuracy in forecasting the removal of MB. Thus, the proposed method promotes enhanced decontamination of the target pollutant within a cost-effective route, contributing to developing sustainable and environmentally friendly remediation technologies.

CRediT authorship contribution statement

Faizan Khan: Writing – original draft, Methodology, Investigation, Formal analysis. **Vishal Singh Pawak:** Validation, Formal analysis. **Chandra Shekhar:** Validation, Formal analysis. **Venkateshwar Rao Dugyala:** Writing – review & editing, Validation. **Tarak Mondal:** Writing – review & editing, Validation. **Manigandan Sabapathy:** Writing – review & editing, Supervision, Resources, Project administration, Funding acquisition, Conceptualization.

Ethics approval:

Not applicable.

Declaration of competing interest

The authors declare that they have no known competing financial interests or personal relationships that could have appeared to influence the work reported in this paper.

Acknowledgments

Data availability

Data will be made available on request.

References

[1] N. Shimizu, C. Ogino, M.F. Dadjour, T. Murata, Sonocatalytic degradation of methylene blue with tio2 pellets in water, Ultrason. Sonochemistry 14 (2) (2007) 184–190.
[2] G.M. ElShafei, F. Yehia, O. Dimitry, A. Badawi, G. Eshaq, Ultrasonic assisted-fenton-like degradation of nitrobenzene at neutral ph using nanosized oxides of fe and cu, Ultrason. Sonochemistry 21 (4) (2014) 1358–1365.
[3] A. Setiawan, L.R. Dianti, N.E. Mayangsari, D.R. Widiana, D. Dermawan, Removal of methylene blue using heterogeneous fenton process with fe impregnated kepok banana (musa acuminate l.) peel activated carbon as catalyst, Inorg. Chem. Commun. 152 (2023) 110715.
[4] P. Alivisatos, The use of nanocrystals in biological detection, Nature Biotechnol. 22 (1) (2004) 47–52.
[5] Y. Wu, D. Wang, Y. Li, Nanocrystals from solutions: catalysts, Chem. Soc. Rev. 43 (7) (2014) 2112–2124.
[6] Z. Zhao, C. Chen, Z. Liu, J. Huang, M. Wu, H. Liu, Y. Li, Y. Huang, Pt-based nanocrystal for electrocatalytic oxygen reduction, Adv. Mater. 31 (31) (2019) 1808115.
[7] G. Konstantatos, E.H. Sargent, Nanostructured materials for photon detection, Nature Nanotechnology 5 (6) (2010) 391–400.
[8] K.M. Mayer, J.H. Hafner, Localized surface plasmon resonance sensors, Chem. Rev. 111 (6) (2011) 3828–3857.
[9] S. Lal, S. Link, N.J. Halas, Nano-optics from sensing to waveguiding, Nat. Photonics 1 (11) (2007) 641–648.
[10] A.F. Koenderink, A. Alu, A. Polman, Nanophotonics: Shrinking light-based technology, Science 348 (6234) (2015) 516–521.
[11] L.N. Quan, J. Kang, C.-Z. Ning, P. Yang, Nanowires for photonics, Chem. Rev. 119 (15) (2019) 9153–9169.
[12] H.S. El-Sheshtawy, K.R. Shoueir, M. El-Kemary, et al., Activated h2o2 on ag/sio2–srwo4 surface for enhanced dark and visible-light removal of methylene blue and p-nitrophenol, J. Alloys Compd. 842 (2020) 155848.
[13] F. Khan, C. Shekhar, T. Mondal, M. Sabapathy, Rapid removal of methylene blue and tetracycline by rough particles decorated with pt nanoparticles, J. Nanoparticle Res. 26 (1) (2024) 4.
[14] A. García, L. Delgado, J.A. Torà, E. Casals, E. González, V. Puntes, X. Font, J. Carrera, A. Sánchez, Effect of cerium dioxide, titanium dioxide, silver, and gold nanoparticles on the activity of microbial communities intended in wastewater treatment, J. Hazard. Mater. 199 (2012) 64–72.
[15] R. Kaegi, A. Voegelin, B. Sinnet, S. Zuleeg, H. Hagendorfer, M. Burkhardt, H. Siegrist, Behavior of metallic silver nanoparticles in a pilot wastewater treatment plant, Environ. Sci. Technol. 45 (9) (2011) 3902–3908.
[16] A. Peter, A. Mihaly-Cozmuta, C. Nicula, L. Mihaly-Cozmuta, A. Jastrzebska, A. Olszyna, L. Baia, Uv light-assisted degradation of methyl orange, methylene blue, phenol, salicylic acid, and rhodamine b: photolysis versus photocatalyis, Water, Air, Soil Pollut. 228 (2017) 1–12.
[17] H.A. Mohammed, S.A. Khaleefa, M.I. Basheer, Photolysis of methylene blue dye using an advanced oxidation process (ultraviolet light and hydrogen peroxide), J. Eng. Sustain. Dev. 25 (1) (2021) 59–67.
[18] A. Ikhlaqa, F. Javedb, A. Niaza, H.M.S. Munirc, F. Qid, Combined uv catalytic ozonation process on iron loaded peanut shell ash for the removal of methylene blue from aqueous solution, Desalination Water Treat. 200 (2020) 231–240.
[19] R. Saleh, A. Taufik, Degradation of methylene blue and congo-red dyes using fenton, photo-fenton, sono-fenton, and sonophoto-fenton methods in the presence of iron (ii, iii) oxide/zinc oxide/graphene (fe3o4/zno/graphene) composites, Sep. Purif. Technol. 210 (2019) 563–573.
[20] T.C. Egbosiuba, A.S. Abdulkareem, A.S. Kovo, E.A. Afolabi, J.O. Tijani, M. Auta, W.D. Roos, Ultrasonic enhanced adsorption of methylene blue onto the optimized surface area of activated carbon: Adsorption isotherm, kinetics and thermodynamics, Chem. Eng. Res. Des. 153 (2020) 315–336.
[21] S. Hsieh, P.-Y. Lin, Fept nanoparticles as heterogeneous fenton-like catalysts for hydrogen peroxide decomposition and the decolorization of methylene blue, J. Nanoparticle Res. 14 (2012) 1–10.
[22] N. Wang, J. Li, L. Ye, X. Li, Heterogeneous nanostructure anatase/rutile titania supported platinum nanoparticles for efficient photocatalytic degradation of methylene blue dyes, Sustain. Chem. Environ. 5 (2024) 100072.
[23] H.J. Huang, L.-Y. Wu, T.-S. Ko, C.-W. Wu, C.-C. Liu, J.-J. Fan, P.-Y. Lee, Y.-S. Lin, Effects of thermal treatment on sea-urchin-like platinum nanoparticlese, Appl. Surf. Sci. 657 (2024) 159799.
[24] M. Chen, J. Zhang, P. Guo, J. Zhai, X. Liu, D. Yu, X. You, J. Li, Pdptcu nanoflower mediated photothermal enhanced fenton catalysis for recyclable degradation of methylene blue, Inorg. Chem. Commun. 160 (2024) 111841.
[25] M. Faisal, J. Ahmed, J.S. Algethami, A.S. Alkorbi, F.A. Harraz, Facile synthesis of platinum/polypyrrole-carbon black/sns2 nanocomposite for efficient photocatalytic removal of gemifloxacin under visible light, J. Saudi Chem. Soc. 28 (2) (2024) 101806.
[26] M.S. Jameel, A.A. Aziz, M.A. Dheyab, B. Mehrdel, Rapid methanol-assisted amalgamation of high purity platinum nanoparticles utilizing sonochemical strategy and investigation on its catalytic activity, Surf. Interfaces 21 (2020) 100785.
[27] Y. Wu, R.N.E. Tiri, M. Bekmezci, E.E. Altuner, A. Aygun, C. Mei, Y. Yuan, C. Xia, E.-N. Dragoi, F. Sen, Synthesis of novel activated carbon-supported trimetallic pt–ru–ni nanoparticles using wood chips as efficient catalysts for the hydrogen generation from nabh4 and enhanced photodegradation on methylene blue, Int. J. Hydrog. Energy 48 (55) (2023) 21055–21065.
[28] D. Peramune, D.C. Manatunga, R.S. Dassanayake, V. Premalal, R.N. Liyanage, C. Gunathilake, N. Abidi, Recent advances in biopolymer-based advanced oxidation processes for dye removal applications: A review, Environ. Res. 215 (2022) 114242.
[29] Y. Ren, S.J. Hersch, X. He, R. Zhou, T.G. Dong, Q. Lu, A lightweight, mechanically strong, and shapeable copper-benzenedicarboxylate/cellulose aerogel for dye degradation and antibacterial applications, Sep. Purif. Technol. 283 (2022) 120229.

[30] Y. Zhang, S. Zhao, M. Mu, L. Wang, Y. Fan, X. Liu, Eco-friendly ferrocene-functionalized chitosan aerogel for efficient dye degradation and phosphate adsorption from wastewater, Chem. Eng. J. 439 (2022) 135605.

[31] S. Giannakis, K.-Y.A. Lin, F. Ghanbari, A review of the recent advances on the treatment of industrial wastewaters by sulfate radical-based advanced oxidation processes (sr-aops), Chem. Eng. J. 406 (2021) 127083.

[32] Y. Wang, C. Feng, Y. Li, J. Gao, C.-P. Yu, Enhancement of emerging contaminants removal using fenton reaction driven by h2o2-producing microbial fuel cells, Chem. Eng. J. 307 (2017) 679–686.

[33] A. Azari, M.H. Mahmoudian, M.H. Niari, I. Eş, E. Dehganifard, A. Kiani, A. Javid, H. Azari, Y. Fakhri, A.M. Khaneghah, Rapid and efficient ultrasonic assisted adsorption of diethyl phthalate onto feiife2iiio4@ go: Ann-ga and rsm-df modeling, isotherm, kinetic and mechanism study, Microchem. J. 150 (2019) 104144.

[34] M. Li, D. Wei, T. Liu, Y. Liu, L. Yan, Q. Wei, B. Du, W. Xu, Edta functionalized magnetic biochar for pb (ii) removal: Adsorption performance, mechanism and svm model prediction, Sep. Purif. Technol. 227 (2019) 115696.

[35] A. Trivedi, S. Hait, Metal bioleaching from printed circuit boards by bio-fenton process: Optimization and prediction by response surface methodology and artificial intelligence models, J. Environ. Manag. 326 (2023) 116797.

[36] K. Zhao, Y. j. Tian, N. y. Deng, Robust unsupervised and semi-supervised bounded *v*- support vector machines, in: Advances in Neural Networks–ISNN 2009: 6th International Symposium on Neural Networks, ISNN 2009 Wuhan, China, May (2009) 26-29 Proceedings, Part II 6, Springer, 2009, pp. 312–321.

[37] D. Knudson, Linear and angular kinematics, in: Fundamentals of Biomechanics, Springer, 2021, pp. 79–100.

[38] S. Sahu, M.K. Yadav, A.K. Gupta, V. Uddameri, A.N. Toppo, B. Maheedhar, P.S. Ghosal, Modeling defluoridation of real-life groundwater by a green adsorbent aluminum/olivine composite: Isotherm, kinetics, thermodynamics and novel framework based on artificial neural network and support vector machine, J. Environ. Manag. 302 (2022) 113965.

[39] A.K. Rathankumar, K. Saikia, M.H. Ribeiro, C.K. Cheng, M. Purushothaman, V. kumar Vaidyanathan, Application of statistical modeling for the production of highly pure rhamnolipids using magnetic biocatalysts: Evaluating its efficiency as a bioremediation agent, J. Hazard. Mater. 412 (2021) 125323.

[40] S. Raj, B. Mahanty, S. Hait, Coagulative removal of polystyrene microplastics from aqueous matrices using fecl3-chitosan system: Experimental and artificial neural network modeling, J. Hazard. Mater. 468 (2024) 133818.

[41] H.E. Hansen, F. Seland, S. Sunde, O.S. Burheim, B.G. Pollet, Two routes for sonochemical synthesis of platinum nanoparticles with narrow size distribution, Mater. Adv. 2 (6) (2021) 1962–1971.

[42] A. Kirchon, P. Zhang, J. Li, E.A. Joseph, W. Chen, H.-C. Zhou, Effect of isomorphic metal substitution on the fenton and photo-fenton degradation of methylene blue using fe-based metal–organic frameworks, ACS Appl. Mater. Interfaces 12 (8) (2020) 9292–9299.

[43] H. Lv, H. Zhao, T. Cao, L. Qian, Y. Wang, G. Zhao, Efficient degradation of high concentration azo-dye wastewater by heterogeneous fenton process with iron-based metal–organic framework, J. Mol. Catal. A: Chemical 400 (2015) 81–89.